Biointerface Research in Applied Chemistry
Open-Access Journal (ISSN: 2069-5837)

*Article*
**Volume 14, Issue 3, 2024, 75**
https://doi.org/10.33263/BRIAC143.075

# Influence of Hydrothermal Temperature Variation and Annealing on ZnO Nanoparticles on the Performance of Photoanode in DSSC

**Gabriel Kwame Sipi Takyi [1,4,*], Emmanuel Nyankson [2], Maxwell Selasse Akple [1], Abu Yaya [2], Gamaralalege Rajanya Asoka Kumara [3], Boateng Onwona-Agyeman [2]**

1 Department of Mechanical Engineering, Ho Technical University, P. O. Box HP 217, Ho, Ghana
2 Department of Materials Science and Engineering, University of Ghana, P. O. Box LG 77, Legon-Accra, Ghana
3 National Institute of Fundamental Studies, Kandy, Peradeniya 20400, Sri Lanka
4 School of Engineering and Sciences, Technologico de Monterrey, Monterrey, N.L., Mexico
* Correspondence: gkstakyi@htu.edu.gh (G.K.S.T.);

Scopus Author ID 57222548961
**Received: 27.06.2023; Accepted: 16.11.2023; Published: 17.02.2024**

**Abstract:** The hydrothermal synthesis method was used to synthesize ZnO nanoparticles at varying temperatures, and the resulting samples were then annealed in air at 500°C. Energy dispersive spectroscopy (EDX), Fourier-transform infrared spectroscopy (FTIR), diffuse reflectance spectroscopy (DRS), and thermogravimetry analysis/differential scanning calorimetry (TGA/DSC) were used to analyze the samples that had been synthesized. With a dominating diffraction peak of (002) at the maximum hydrothermal temperature of 120°C and the annealing temperature of 500°C for 30 minutes, the XRD data show the development of hexagonal wurtzite phases. The EDX results showed the presence of elemental zinc and oxygen, whereas the SEM revealed almost spherical particles with improved agglomeration. For the sample synthesized at 120°C and annealed at 500°C, FTIR examination shows that volatile organic compounds have been removed from the sample. The light-to-electric energy conversion efficiency was recorded to be 1.4 % for ruthenium-based complex (N719) dye and 1% for metal-free indoline (D149) dye under AM 1.5 irradiation (1000 Wm-2 simulated sunlight) when the ZnO nanoparticles prepared at 120°C was combined with colloidal tin oxide to form a composite-photoanode in dye-sensitized solar cells.

**Keywords:** zinc oxide; hydrothermal; annealing; solar cell; SEM; DSSC.



## 1. Introduction

A renewable energy source, photovoltaic (PV), uses solar cells to convert sunlight into electricity [1,2]. Over the past few decades, semiconductor materials exhibiting the photovoltaic effect have drawn much interest [3]. Silicon, cadmium telluride (CdTe), tin oxide ($SnO_2$), titanium dioxide ($TiO_2$), and zinc oxide (ZnO) are a few examples of semiconducting materials that are actively exploited in solar applications [4-6].

Generally, solar cells are classified into three (3) generations. The first generation of solar cells is based on silicon crystals like monocrystalline and polycrystalline silicon [7, 8]. The second generation of solar cells is made of thin sheets like amorphous silicon, copper-indium-gallium-selenide (CIGS), and cadmium telluride (CdTe) [9, 10]. The third generation's most common type of solar cell is dye-sensitized solar cells (DSC) [11-13]. The DSC has

garnered a lot of research interest due to its low production costs and flexibility of production [11, 14-16].

A porous wide bandgap semiconductor is deposited on an electrode of a transparent n-type semiconductor to produce the DSC. This porous semiconductor is made with a wide surface area specifically for supporting a monolayer of dye on its surface. The dye sensitizer is the absorber of sunlight in the DSC, and the efficient conversion of light into electrical energy is made possible by the porous semiconductor by transporting the photo-injected electron to the transparent electrode [17-19]. $TiO_2$ is one of the porous wide bandgap semiconductors commonly used as DSC photoanode [16, 17]. Due to the numerous grain boundaries and disordered grain network, it exhibits weak electron mobility, slow transport, and potential for photo-excited electron and hole recombination despite its large surface area. ZnO is more widely available, less expensive, non-toxic, and has excellent chemical and thermal stability in addition to having similar properties to $TiO_2$. ZnO nanostructures and $TiO_2$ exhibit similar energy band structures and physical properties, making it a potential candidate for use as a photo-anode. [20, 21].

ZnO nanopowders can be prepared by several physical and chemical synthesis techniques such as mechano-chemical-thermal synthesis [20], spray pyrolysis [21], laser ablation [22], electrochemical depositions, sol-gel method, microwave synthesis, and chemical-precipitation methods [23-33]. However, most of these synthesis methods need high-temperature processing, which typically causes some volatile molecules in the sample to evaporate. [26, 34].

The hydrothermal method is a chemical synthesis method that takes place in a closed system at low temperatures and atmospheric pressure. Modifications in the source species (concentrations of reactants), reaction time, and temperature regulate the prepared material's particle properties, including morphology and size [24, 25, 28].

The defects in the ZnO NPs are greatly influenced by the annealing and the conditions under which ZnO is prepared [32, 35, 36]. On thin films and nanostructured ZnO, the impact of annealing conditions on defect-related emissions has been thoroughly investigated [37-39]. The annealing improves the material's electrical and optical properties, which also removes internal tension in the ZnO [38, 40, 41]. Previous studies have shown that air-annealed ZnO is a viable candidate for photodetector applications due to its low dark current [40, 42-44]. However, DSCs are known to have low sunlight-to-electric power conversion efficiency, but the conversion efficiency can be improved by forming a composite photoanode with an oxide semiconductor such as tin oxide [45, 46].

Although the hydrothermal synthesis method is a well-established process and has been used to produce several ZnO particles for other applications, the effect of varying the hydrothermal temperature, as well as annealing, has not been studied for DSSC applications.

It is, therefore, important to study the effect of different preparation temperatures and post-deposition annealing conditions for ZnO particles using the hydrothermal method.

The novelty in this work is the variation of the hydrothermal temperatures, annealed at 500℃ and characterized. The resulting ZnO was used as a composite photoanode in a DSC to evaluate the solar cell performance.

## 2. Materials and Methods

Zinc acetate dihydrate, sodium hydroxide, and methanol used in this work were of analytical grade and were used as purchased from Sigma Aldrich.

*2.1. Synthesis of ZnO.*

50ml of methanol was stirred to produce a 0.5M zinc acetate solution. Adding 25ml of 1M NaOH dropwise while stirring continuously at room temperature formed a clear, white solution that eventually turned milky. Using NaOH, the pH of the mixture was brought down to 8. The hydrothermal treatment was carried out in a Teflon-lined stainless steel autoclave using four different temperatures (90, 100, 110, and 120°C) for six hours at a pressure of 400kPa. [25, 41].

Methanol was used to wash the finished product after it had cooled to room temperature, filter it, and then dry it in a lab oven at 60°C. A portion of each prepared sample was annealed for 30 minutes at 500°C in a Thermolyne oven. The formation of the ZnO nanoparticles from this synthesis method can be described by the reactions below [41]:

$$Zn(CH_3COO)_2.2H_2O + 2NaOH \rightarrow Zn(OH)_2 + 2CH_3COONa + 2H_2O \quad (1)$$

$$Zn(OH)_2(gel) + 2H_2O = Zn^{2+} + 2OH^- + 2H_2O + [\,Zn(OH)_4]^2 \quad (2)$$

$$[Zn(OH)_4]^{2-} \rightarrow ZnO_2^{2-} + 2H_2O \quad (3)$$

$$ZnO_2^{2-} + 2H_2O \rightarrow ZnO + 2OH^- \quad (4)$$

The growth mechanism of the zinc oxide nanostructure is a complex process. This usually comprises two main steps: the generation of the nuclei and the subsequent crystal growth of the nuclei forming the zinc oxide. The $Zn(OH)_4^{2-}$ complexes are basic growth units for preparing zinc oxide nanostructures [41]. ZnO nuclei will form following reaction (4) when the concentration of $Zn^{2+}$ and $OH^-$ reaches a supersaturation degree.

*2.2. Construction of DSC.*

Porous ZnO-composite films were prepared on two (2) fluorine-doped tin oxide (FTO) coated glass (sheet resistance ~ 8Ω /sq and transmittance ~ 80%) by mixing 0.6g of the ZnO nanoparticles (synthesized at 120°C and annealed at 500°C), with 2 ml of colloidal tin oxide, few drops of glacial acetic acid and ethanol (40ml) and ultrasonically dispersing the solution for 10 min [45]. The mixture was then sprayed onto heated FTO glass at 150°C using a spray gun and annealed to the resultant film at 500°C in the air for 30 minutes. The ZnO-composite photoanodes (active area ~ 0.25$cm^2$) were then immersed in a separate mixture of acetonitrile and *tert*-butanol (volume 1:1) containing indoline dye D149 (Mitsubishi Paper Mills) and Ru-based dye N719 (Solaronix) for 5 hrs [47]. The dye-coated ZnO electrodes were removed, rinsed with acetonitrile, and allowed to dry in air. Construction of the DSC was carried out by sandwiching the dye-coated ZnO electrode with a sputtered platinum-coated counter electrode and the intervening space filled with an electrolyte (electrolyte composition: 0.1M LiI, 0.05M $I_2$, 0.6M dimethyl propyl-imidazolium iodide in methoxyacetonitrile). The current-voltage (*I–V*) characteristics of the cells at AM 1.5 (1000 $Wm^{-2}$) simulated sunlight irradiation were recorded with a calibrated solar cell evaluation system (PECell-PEC L-12, Japan).

*2.3. Characterization.*

X-ray diffraction studies (Bruker D8 theta) were carried out using Cu-filtered K$\alpha$ radiation (wavelength = 0.154060nm) as the x-ray source in the 2$\theta$ range of 20◦ to 80◦. Also, the diffraction peaks obtained in the XRD measurement were analyzed based on a curve-fitting method by using standard software within the workstation.

Fourier transform infrared (FTIR) spectroscopy was used to identify the functional groups of the synthesized ZnO nanoparticles in the range of 4,000 - 500$cm^{-1}$.

An EDX acquisition detector fitted to a field emission scanning electron microscope (Nova NanoSEM 450) was used to examine the samples' morphology and elemental composition (5-15KeV; 4.8 – 6.9nm). A diffuse reflectance spectrophotometer (An Ocean Optics USB-400) with a dedicated reflectance probe was used to analyze the optical properties of the prepared samples. Illumination from a Halogen/Deuterium source was used across the UV-Vis range, and Kubelka-Munk's function was used to calculate the band gap of the samples.

Using the differential scanning calorimetry and thermal gravimetric analysis instrument (DSC/TG, ATQ 500), the thermal properties of the samples were ascertained.

An alumina crucible containing 22.3mg of the sample was heated to 800°C at a 10K/min heating rate.

## 3. Results and Discussion

### *3.1. Sample identification.*

Four (4) samples were prepared at different hydrothermal temperatures (i.e., 90, 100, 110, and 120°C), and all were subsequently annealed. The samples with A preceding their names denote the As-prepared samples without annealing, while those with C denote the samples that have been annealed in air at 500℃ for 30 minutes.

- The As-prepared samples are A90, A100, A110, and A120.
- The annealed samples are C90, C100, C110, and C120.

### *3.2. X-ray diffraction analysis (XRD).*

The XRD patterns obtained for the as-prepared and annealed samples are shown in Figure 1 and Figure 2, respectively. The XRD peaks formed in the as-prepared samples became sharp with increasing hydrothermal temperatures, while the crystallinity of the samples also improved with increasing hydrothermal temperatures, with (101) being the dominant peak in the samples prepared at 110 and 120°C. In the case of the annealed samples, the (101) peak dominated in samples prepared at 90, 100, and 110°C, but the sample prepared at 120°C exhibited a dominant XRD peak of (002). No other phases were present, which suggested the high-purity samples were obtained after annealing. These characteristic diffraction peaks of the samples shown in Figures 1 and 2 indicate the hexagonal wurtzite structure [48-50].

Although zinc oxide powders were directly synthesized during the hydrothermal process, it was observed that the XRD peaks were not distinct in the as-prepared samples and were relatively amorphous in structure at lower hydrothermal temperatures. The peaks became more distinct and sharper with increasing hydrothermal temperatures and at an annealing temperature of 500℃. This is because the nucleation and growth of zinc oxide crystals depend on the hydrothermal conditions and annealing temperatures.

In Figure 2, it was observed that the sample synthesized hydrothermally at 120℃ and the annealing temperature of 500℃ for 30 minutes shows a high degree of preferential orientation of the (002) diffraction peak, while the other samples show the preferential orientation of the (001) diffraction peak. The most dominant peak at 34.39° corresponding to (002) crystallographic plane indicates that the nanoparticles preferentially grow along the c-axis crystal plane of the ZnO Wurtzite structure when zinc oxide is prepared at a hydrothermal

temperature of 120℃ followed by annealing in air at 500°C for 30 minutes. The high intensity of the (002) diffraction peak is crucial and significant for optoelectronic applications such as solar cells [48, 51].

The crystallite sizes of the samples were calculated using the Derby-Scherer equation (Equation 5), and the data are listed in Table 1.

$$d = \frac{k\lambda}{\beta \cos\theta} \qquad (5)$$

Where d, λ, β, and Θ are the crystal size, x-ray wavelength (0.154nm), Scherer constant (0.89), β is the full width at half maximum (FWHM), and the Bragg angle, respectively.

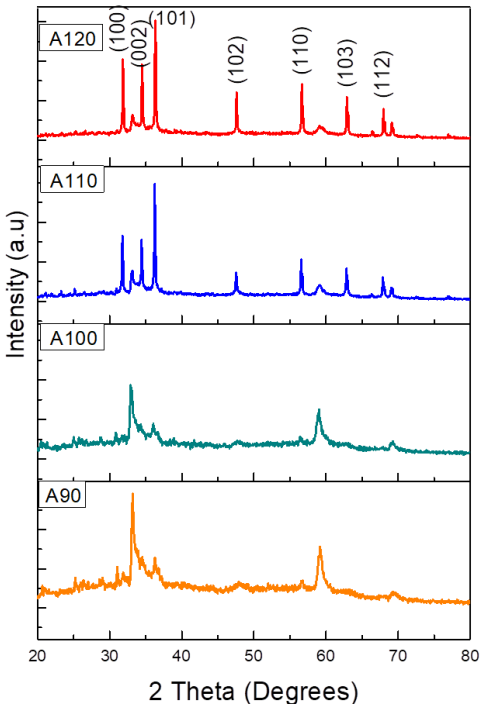


**Figure 1.** XRD patterns of As-prepared samples with different hydrothermal temperatures.

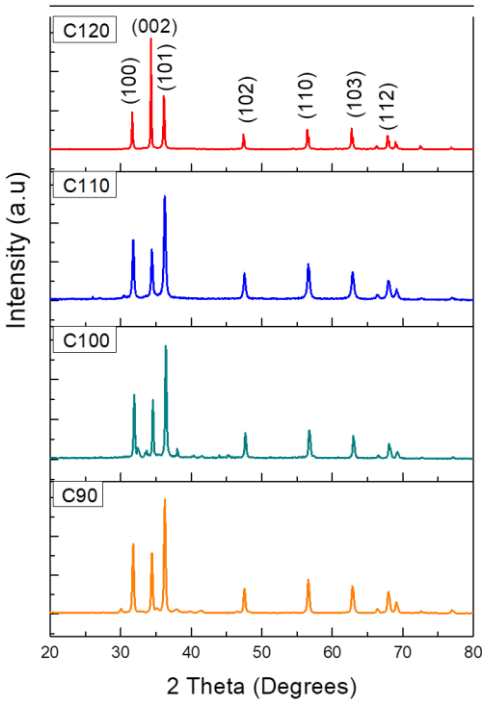


**Figure 2**. XRD patterns of annealed samples with different hydrothermal temperatures.

**Table 1**. Average crystallite size and other parameters derived from the XRD data.

| Sample | 002 Peak position 2θ (°) | FWHM 2θ (°) | Crystallite size (nm) |
|---|---|---|---|
| C90 | 36.26 | 0.28 | 31.13 |
| C100 | 36.41 | 0.25 | 33.90 |
| C110 | 36.27 | 0.33 | 25.77 |
| C120 | 34.31 | 0.16 | 54.64 |

*3.3. Fourier transform infrared analysis (FTIR).*

The FTIR analysis was conducted on the samples to identify the organic and inorganic functional groups in the prepared samples.

Figures 3 and 4 show the FTIR analysis of the as-prepared and annealed samples, respectively. The peak corresponding to the Zn-O bond vibration at 531cm$^{-1}$ wave number was observed [15, 51]. The broad peak at 3438cm$^{-1}$ can be attributed to the presence of symmetric vibrations of –OH (hydroxyl groups) and C = O [52, 53]. This is due to the atmospheric moisture and molecules of $CO_2$, respectively. The C=O peak could have also resulted from the zinc acetate precursor used in the synthesis. The absorption bands at 1050-1650cm$^{-1}$ imply the presence of stretching vibrations of the CO-Zn and the –OH group on the surface of ZnO nanoparticles. This result is similar to those reported in the literature [41, 48-52].

It can also be observed in Figure 4 that annealing the samples removed all the organic compounds and the molecules of water present. This is in line with the observation made by XRD as the samples became more crystalline with sharper peaks. The results from the XRD and FTIR confirmed the synthesis of high-purity ZnO nanoparticles.

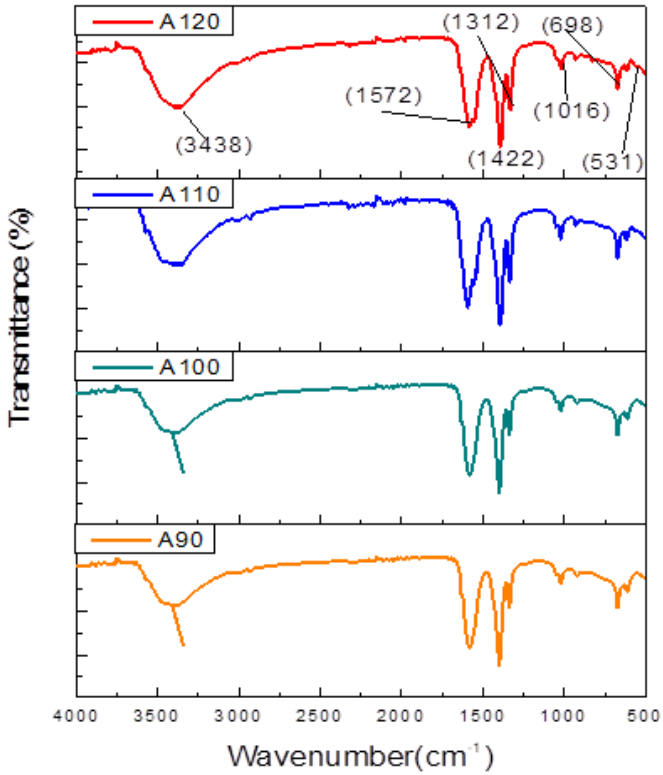


**Figure 3**. FTIR spectra of As-prepared samples with varying hydrothermal temperatures.

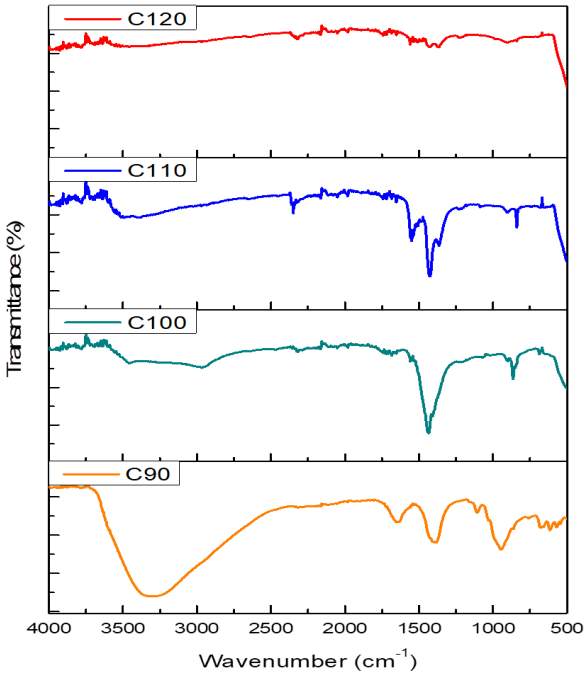


**Figure 4**. FTIR spectra of annealed samples varying hydrothermal temperatures.

*3.4. Scanning electron microscope.*

The surface morphology of the samples was determined using an SEM, as shown in Figure 5, and the images show the formation of spherical nanoparticles. The spherical morphology of the particles became distinct after annealing. It was also observed that the degree of agglomeration of the as-prepared and annealed samples increased with increasing hydrothermal temperatures. The agglomeration observed can be attributed to the fact that surfactants were not used in this work [54].

It was also observed that well-defined particles were formed when the samples were annealed at 500℃ for 30 minutes.

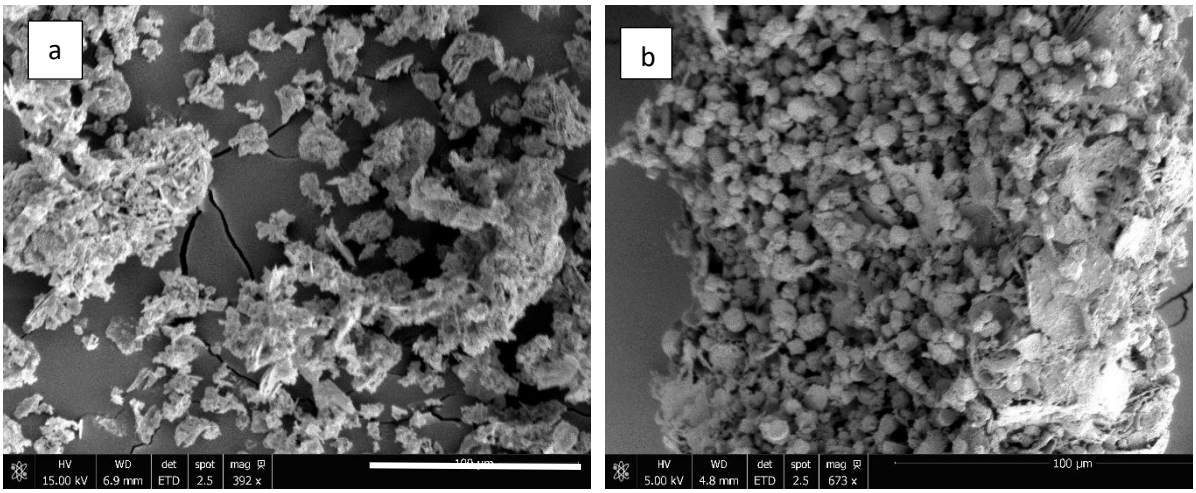


**Figure 5**. SEM images of the samples hydrothermally prepared at 120℃ **(a)** as-prepared; **(b)** annealed at 500℃ for 30 minutes.

*3.5. Energy dispersive spectroscopy (EDX).*

The elemental compositions of the ZnO nanoparticles were observed using energy-dispersive X-ray spectroscopy, as shown in Figure 6. The same peaks (for Zn and O) for all

samples were observed in the EDX data, confirming the formation of ZnO. Figure 6 shows the EDX spectra of the C120 sample. It was observed that increasing the hydrothermal temperature in both the as-prepared and the annealed samples increases the weight/atomic percent of the zinc, as indicated in Table 2. This implies that a highly crystalline and pure ZnO is prepared when annealed (500°C) at the hydrothermal temperature of 120°C as compared to the theoretical mass percent composition of Zn and O in ZnO to be 80.34% and 19.66%, respectively using molecular weight calculation. The unidentified peak at 2KeV corresponds to the Pt used in the sputter coating of the samples.

**Table 2**. Elemental composition of the C120 and A120 (in brackets) samples.

| Element | Weight % | Atomic % |
|---|---|---|
| Zn K | 89.65(78.60 ) | 67.94(47.33) |
| O K | 10.35(21.40) | 32.06(52.67) |
| Total | 100 | 100 |

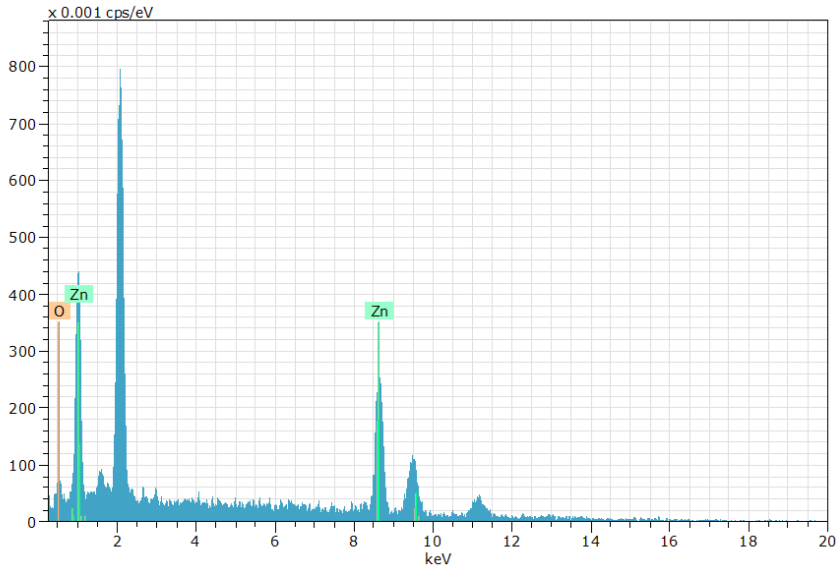


**Figure 6**. EDX of Annealed sample at 120°C (C120) showing the elemental composition of the sample.

*3.6. Diffuse reflectance spectroscopy (DRS).*

The effect of the different hydrothermal temperatures on the as-prepared and annealed ZnO samples on the optical properties of ZnO nanoparticles was investigated.

1. Figures 7 and 8 show the diffuse reflectance and the modified Kubelka-Munk plots of the as-prepared and annealed samples. It is observed that there is a significant decrease in reflectance in all the annealed samples, which implies an increase in light absorption when the samples were annealed at 500℃.
2. It can be seen from Figure 7 that the absorbance of light shifted to a relatively higher wavelength after annealing. The optical band was estimated using the Kubelka-Munk equation in the limiting case of an infinitely thick sample at any wavelength [49, 54-58] using the relation;

$$\frac{K}{S} = \frac{(100-R)^2}{2R} = F(R) \qquad (6)$$

Where F(R) is the remission or Kubelka-Munk function (K-M), S is K-M scattering coefficients, R is reflectance, and K is the absorption coefficients.

For a material that scatters in a perfectly diffuse manner, the K-M absorption coefficient K becomes 2α (K=2α)

The bandgap energy $E_g$ and coefficient α of a direct bandgap semiconductor are related through the equation;

$$\alpha hv = B(hv - E_g)^{\frac{1}{2}} \quad (7)$$

Where α is the linear absorption coefficient of the material hv is the photon energy, and B is a proportionality constant.

Considering the K-M scattering coefficients S as a constant concerning the wavelength and combining and rearranging equations 6 and 7, equation 8 below was obtained

$$[F(R)hv]^2 = B(hv - E_g) \quad (8)$$

The bandgap energies of the samples are then measured by extrapolating the linear portion of the graph between the modified Kubelka-Munk (K-M) function versus the photon energy (hv).

The extrapolation of the straight lines in Figure 8 gives the value of the bandgap energies. It was found that the optical bandgap of the samples increased when they were annealed. There is an increase in the optical bandgap of the semiconductor when particle size decreases [59]. Table 3 shows the estimated optical band gaps of the as-prepared samples and the annealed samples.

The bandgap of the samples did not show any significant changes when they were annealed except for the sample, which was hydrothermally synthesized at a temperature of 110℃ where the bandgap measured was slightly lower.

**Table 3**. Band gaps of the as-prepared and annealed ZnO particles.

| As-prepared samples | Bandgap (eV) | Annealed samples | Bandgap (eV) |
|---|---|---|---|
| A100 | 3.1 | C100 | 3.2 |
| A110 | 3.2 | C110 | 3.1 |
| A120 | 3.2 | C120 | 3.2 |

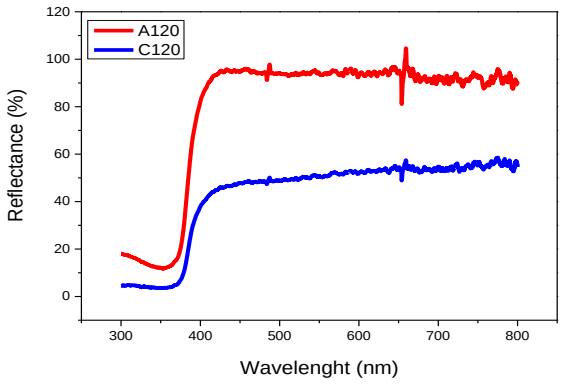


**Figure 7**. DRS of As-prepared sample A120 and Annealed sample C120.

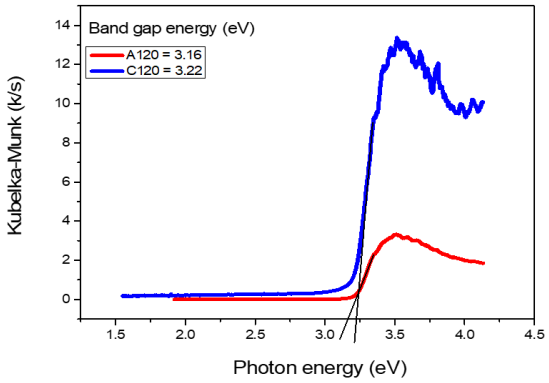


**Figure 8**. The Kubelka-Munk plots of the As-prepared sample A120 and Annealed sample C120.

*3.7. Thermogravimetric analysis (TGA) and differential scanning calorimetry (DSC).*

As shown in Figure 9, TGA and DSC were utilized to determine the thermal characteristics of the samples, and the TGA/DSC patterns were consistent across all samples evaluated.

The emergence of an exothermic peak around 150°C corresponds to the elimination of water of crystallization in the sample, resulting in a 10% weight loss. The weight loss continues to increase with temperature until it reaches 380°C. At this point, an endothermic peak is produced, corresponding to the decomposition and combustion of the organic bonds in the sample. No appreciable weight loss was observed above 380°C, indicating that the ZnO nanoparticles are stable [11].

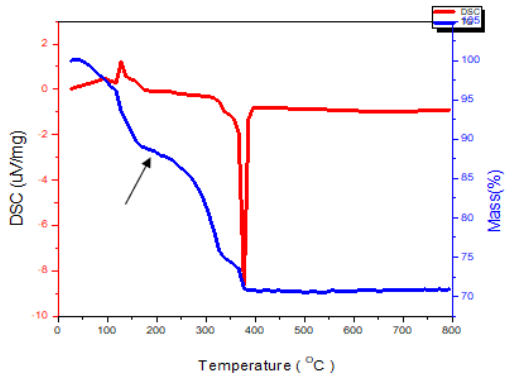


**Figure 9.** DSC/TG analysis of ZnO at hydrothermal temperature 120°C (A120). The arrow on the TGA curve indicates the initial water loss of crystallization.

*3.8. Photoanode material properties and I-V measurements.*

For a nanocrystalline semiconductor to be used as an efficient photoanode in a porous-structured solar cell such as DSC, the surface structure of the semiconductor must be designed to give rise to the presence of electron pathways where photo-injected electrons from the dye sensitizer can travel through the porous photoanode to the external circuit. Such pathways can be created within the semiconductor network by sintering or heat-treating the semiconductor particles, resulting in efficient electrical contact between the nanoparticles. This sintering treatment improves charge percolation through the porous nanoparticle network and facilitates the solar cell's high light-to-charge conversion efficiency. Also, it has been established that electron transport in nanocrystalline porous semiconductor film in a DSC is dominated by electron trapping within the bandgap defect states [60]. The porous semiconductor must exhibit some degree of particle interconnection to allow percolation of injected electrons, and the crystallinity of the porous film (and the extent of defects) also influences the transport of injected electrons through the network of particles in the film to the collecting electrode. Any defect structure that disrupts the flow of injected electrons through the porous semiconductor greatly affects the current-voltage (*I–V*) parameters and, hence, the conversion efficiency of the DSC.

**Table 4.** *I-V* parameters of ZnO-composite DSC sensitized with D149 and N719 dyes respectively.

| Dye | Voc (mV) | FF (%) | Jsc (A/cm$^2$) | Efficiency (%) |
|---|---|---|---|---|
| N719 | 654 | 71 | 2.9 | 1.4 |
| D149 | 707 | 77 | 1.76 | 1 |

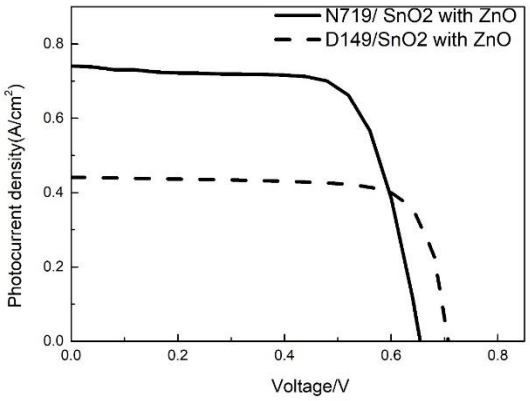


**Figure 10**. *I-V* characteristics of ZnO-composite photoanode sensitized with D149 and N719 dyes.

The ZnO nanoparticles synthesized at 120°C were used to fabricate two (2) DSCs and sensitized with metal-free D149) and Ru-based (N719) dyes, respectively. Figure 10 shows the photovoltaic performance of the DSCs, and Table 4 summarizes the results where Jsc is the short-circuit photocurrent density under irradiation, Voc is the open-circuit voltage, and FF is the fill factor. From Table 4, the solar energy conversion efficiency of the DSC sensitized with the Ru-based dye is higher than that of the indoline dye (D149) DSC [61]. Generally, the conversion efficiency of a solar cell is given by [62];

$$\eta = \frac{FF \times Jsc \times Voc}{Pin} \quad (9)$$

where $P_{in}$ is the incident light intensity (1000Wm$^{-2}$). Since the difference in the values of Voc and FF recorded for the two solar cells was small, the Jsc determined the conversion efficiency of the solar cells. The Jsc measures the sensitized electrode's light-harvesting ability and results in high photocurrent density in the solar cell. From Table 4, the ZnO-composite photoanode sensitized with the indoline dye recorded Jsc of 1.76A/cm$^{2,}$ while the ZnO-composite photoanode sensitized with N719 recorded Jsc of 2.9A/cm$^2$. The higher photocurrent recorded by the Ru-sensitized ZnO photoanode indicates the better light-harvesting capability of Ru dye on the hydrothermally prepared ZnO. Previously, a screen-printed ZnO electrode on an AZO-coated glass substrate sensitized with eosin dye yielded a conversion efficiency of 0.61% [63]. Also, ZnO nanowire electrodes on AZO-coated glass substrate sensitized with a ruthenium complex dye gave an overall conversion efficiency of 0.6% [64]. Therefore, the hydrothermally synthesized ZnO nanoparticles sensitized with a metal-free dye (D149) can potentially be used as a photoanode in DSCs.

## 4. Conclusions

ZnO nanoparticles were synthesized successfully by the hydrothermal technique using different hydrothermal temperatures and annealed at a temperature of 500℃ for 30 minutes. XRD, SEM, EDX, DRS, FTIR, and TGA characterized the synthesized nanoparticles.

The XRD and EDX results confirm the crystalline nature, hexagonal wurtzite structure, and elemental composition of the ZnO NPs. ZnO NPs prepared by the hydrothermal treatment at 120℃ and annealing at 500℃ for 30 minutes showed the highest (002) diffraction peak as required for optoelectronic devices such as in the nanostructured solar cell.

The FTIR and the DSC/TG analysis indicate the effect of the annealing on the synthesized samples as water molecules and organic compounds are removed with increasing hydrothermal temperature. Using ZnO nanoparticles prepared at 120°C and mixed to form composite-photoanode in DSCs sensitized with metal-free (D149) and Ru-based (N719) dyes,

conversion efficiencies of 1 and 1.4% were recorded. The higher efficiency recorded for the ruthenium-sensitized photoanode is attributed to better light harvesting, resulting in the high photocurrent density of the Ru-sensitized ZnO-composite photoanode.

## Funding

This research received no external funding.

## Acknowledgments

Prof. Nyankson would like to acknowledge Cambridge University's support for using some characterization instruments.

## Conflicts of Interest

The authors declare that they have no conflict of interest. They contributed equally to the success of the work.

## References

1. Ranabhat, K.; Patrikeev, L.; Antal'evna, R.A.; Andrianov, K.; Lapshinsky, V.; Sofronova, E. An introduction to solar cell technology. *J. Appl. Eng. Sci.* **2016**, *14*, 481-491, https://doi.org/10.5937/jaes14-10879.
2. Kant, N.; Singh, P. Review of next generation photovoltaic solar cell technology and comparative materialistic development. *Mater. Today: Proc.* **2016**, *56*, 3460-3470, https://doi.org/10.1016/j.matpr.2021.11.116.
3. Khare, V.; Nema, S.; Baredar, P. Status of solar wind renewable energy in India. *Renew. Sust. Energy Rev.* **2013**, *27*, 1-10, https://doi.org/10.1016/j.rser.2013.06.018.
4. Efaz, E.T.; Rhaman, M.M.; Al Imam, S.; Bashar, K.L.; Kabir, F.; Mourtaza, E.; Sakib, S.N.; Mozahid, F.A. A review of major technologies of thin-film solar cells. *Eng. Res. Express* **2021**, *3*, 032001, https://doi.org/10.1088/2631-8695/ac2353.
5. Papadimitriou, D.N.; Roupakas, G.; Roumeliotis, G.G.; Vogt, P.; Köhler, T. Optimization of Electrochemically Deposited Highly Doped ZnO Bilayers on Ga-Rich Chalcopyrite Selenide for Cost-Effective Photovoltaic Device Technology. *Energies* **2016**, *9*, 951, https://doi.org/10.3390/en9110951.
6. Alarifi, I.M. Advanced selection materials in solar cell efficiency and their properties-A comprehensive review. *Mater. Today: Proc.* **2021**, *81*, 403-414, https://doi.org/10.1016/j.matpr.2021.03.427.
7. Yuliantini, L.; Angel, J.; Ramadhan, M.D.; Parwatiningtyas, D. Study of polycrystalline silicon solar cell structure by XRD and SEM characterization. *AIP Conf. Proc.* **2023**, *2619*, 050015, https://doi.org/10.1063/5.0123081.
8. Prishya, A.S.A.; Chopra, L.; Monikanika. Comprehensive review on uses of silicon dioxide in solar cell. *Mater. Today: Proc.* ***2023***, *72*, 1471-1478, https://doi.org/10.1016/j.matpr.2022.09.348.
9. Hashmi, G.; Hossain, M.S.; Imtiaz, M.H. Electrical and optical parameter-based numerical simulation of high-performance CdTe, CIGS, and CZTS solar cells. *J. Theor. Appl. Phys.* **2023**, *17*, 1-15, http://doi.org/10.57647/J.JTAP.2023.1703.28.
10. Ebhota, W.; Tabakov, P. Influence of photovoltaic cell technologies and elevated temperature on photovoltaic system performance. Ain Shams Engineering Journal **2023,** 14, 101984, https://doi.org/10.21203/rs.3.rs-597980/v1.
11. Zi, M.; Zhu, M.; Chen, L.; Wei, H.; Yang, X.; Cao, B. ZnO photoanodes with different morphologies grown by electrochemical deposition and their dye-sensitized solar cell properties. *Ceram. Int.* **2014**, *40*, 7965-7970, https://doi.org/10.1016/j.ceramint.2013.12.146.
12. Ebenezer Anitha, A.; Dotter, M. A Review on Liquid Electrolyte Stability Issues for Commercialization of Dye-Sensitized Solar Cells (DSSC). *Energies* **2023**, *16*, 5129, https://doi.org/10.3390/en16135129.
13. Dei Bukari, S.; Balanay, M.P.; Baptayev, B. Cost-effective and high-performance dye-sensitized solar cells using polymer-based counter electrodes. **2023**, http://nur.nu.edu.kz/handle/123456789/7169.

14. Chou, H.-T.; Hsu, H.-C. The effect of annealing temperatures to prepare ZnO seeds layer on ZnO nanorods array/TiO2 nanoparticles photoanode. *Solid-State Electron.* **2016**, *116*, 15-21, https://doi.org/10.1016/j.sse.2015.11.004.
15. Hussein, A.M.; Iefanova, A.V.; Koodali, R.T.; Logue, B.A.; Shende, R.V. Interconnected $ZrO_2$ doped $ZnO/TiO_2$ network photoanode for dye-sensitized solar cells. *Energy Rep.* **2018**, *4*, 56-64, https://doi.org/10.1016/j.egyr.2018.01.007.
16. Sadikin, S.N.; Rahman, M.Y.A.; Umar, A.A. $TiO_2$-$BaTiO_3$ Composite Films as Photoanode for Dye Sensitized Solar Cell: Effect of $BaTiO_3$ Content. *J. New Mater. Electrochem. Syst.* **2017**, *20*, 109-113, https://doi.org/10.14447/jnmes.v20i3.325.
17. Park, S.K.; Han, Y.S. Efficient dye-sensitized solar cells with surface-modified photoelectrodes. *Sol. Energy* **2014**, *110*, 260-267, https://doi.org/10.1016/j.solener.2014.09.019.
18. Lu, L.; Li, R.; Fan, K.; Peng, T. Effects of annealing conditions on the photoelectrochemical properties of dye-sensitized solar cells made with ZnO nanoparticles. *Sol. Energy* **2010**, *84*, 844-853, https://doi.org/10.1016/j.solener.2010.02.010.
19. Jiang, C.Y.; Sun, X.W.; Lo, G.Q.; Kwong, D.L.; Wang, J.X. Improved dye-sensitized solar cells with a ZnO-nanoflower photoanode. *Appl. Phys. Lett.* **2007,** *90*, 263501, https://doi.org/10.1063/1.2751588.
20. Hui, X.; Kui, H. Effects of $TiO_2$ and ZnO nanoparticles on vermicomposting of dewatered sludge: studies ased on the humification and microbial profiles of vermicompost. *Environ. Sci. Pollut. Res.* **2021**, *28*, 38718-38729, https://doi.org/10.1007/s11356-021-13226-9.
21. Javed, H.M.A.; Adnan, M.; Qureshi, A.A.; Javed, S.; Adeel, M.; Akram, M.A.; Shahid, M.; Ahmad, M.I.; Afzaal, M.; Abd-Rabboh, H.S.M.; Arif, M. Morphological, structural, thermal and optical properties of Zn/Mg-doped $TiO_2$ nanostructures for optoelectronic applications. *Opt. Laser Technol.* **2022**, *146*, 107566, https://doi.org/10.1016/j.optlastec.2021.107566.
22. Mostafa, A.M. Preparation and study of nonlinear response of embedding ZnO nanoparticles in PVA thin film by pulsed laser ablation. *J. Mol. Struct.* **2021**, *1223*, 129007, https://doi.org/10.1016/j.molstruc.2020.129007.
23. Forouzandeh, P.; Ganguly, P.; Dahiya, R.; Pillai, S.C. Supercapacitor electrode fabrication through chemical and physical routes. *J. Power Sources* **2022**, *519*, 230744, https://doi.org/10.1016/j.jpowsour.2021.230744.
24. Shivaraj, B.; Prabhakara, M.C.; Bhojya Naik, H.S.; Indrajith Naik, E.; Viswanath, R.; Shashank, M.; Kumara Swamy, B.E Optical, bio-sensing, and antibacterial studies on Ni-doped ZnO nanorods, fabricated by chemical co-precipitation method. *Inorg. Chem. Commun.* **2021**, *134*, 109049, https://doi.org/10.1016/j.inoche.2021.109049.
25. Noman, M.T.; Amor, N.; Petru, M.; Mahmood, A.; Kejzlar, P. Photocatalytic Behaviour of Zinc Oxide Nanostructures on Surface Activation of Polymeric Fibres. *Polymers* **2021**, *13*, 1227, https://doi.org/10.3390/polym13081227.
26. Baxter, J.B.; Walker, A.M.; van Ommering, K.; Aydil, E.S. Synthesis and characterization of ZnO nanowires and their integration into dye-sensitized solar cells. *Nanotechnology* **2006**, *17*, S304, https://doi.org/10.1088/0957-4484/17/11/S13.
27. Singh, T.A.; Sharma, A.; Tejwan, N.; Ghosh, N.; Das, J.; Sil, P.C. A state of the art review on the synthesis, antibacterial, antioxidant, antidiabetic and tissue regeneration activities of zinc oxide nanoparticles. *Adv. Colloid Interface Sci.* **2021**, *295*, 102495, https://doi.org/10.1016/j.cis.2021.102495.
28. Kannan, K.; Radhika, D.; Kasai, R.D.; Gnanasangeetha, D.; Palani, G.; Gurushankar, K.; Koutavarapu, R.; Lee, D.-Y.; Shim, J. Facile fabrication of novel ceria-based nanocomposite (CYO-CSO) via co-precipitation: Electrochemical, photocatalytic and antibacterial performances. *J. Mol. Struct.* **2022**, *1256*, 132519, https://doi.org/10.1016/j.molstruc.2022.132519.
29. Erol, A.; Okur, S.; Comba, B.; Mermer, Ö.; Arıkan, M.Ç. Humidity sensing properties of ZnO nanoparticles synthesized by sol–gel process. *Sens. Actuators B: Chem.* **2010**, *145*, 174-180, https://doi.org/10.1016/j.snb.2009.11.051.
30. Saleem, S.; Jameel, M.H.; Akhtar, N.; Nazir, N.; Ali, A.; Zaman, A.; Rehman, A.; Butt, S.; Sultana, F.; Mushtaq, M.; Zeng, J.H.; Amami, M.; Althubeiti, K. Modification in structural, optical, morphological, and electrical properties of zinc oxide (ZnO) nanoparticles (NPs) by metal (Ni, Co) dopants for electronic device applications. *Arab. J. Chem.* **2022**, *15*, 103518, https://doi.org/10.1016/j.arabjc.2021.103518.
31. Lu, C.-H.; Yeh, C.-H. Influence of hydrothermal conditions on the morphology and particle size of zinc oxide powder. *Ceram. Int.* **2000**, *26*, 351-357, https://doi.org/10.1016/s0272-8842(99)00063-2.

32. Rayerfrancis, A.; Bhargav, P.B.; Ahmed, N.; Chandra, B.; Dhara, S. Effect of pH on the morphology of ZnO nanostructures and its influence on structural and optical properties. *Phys. B: Condens. Matter* **2015**, *457*, 96-102, https://doi.org/10.1016/j.physb.2014.09.044.
33. Hammad, T.M.; Salem, J.K.; Harrison, R.G. The influence of annealing temperature on the structure, morphologies and optical properties of ZnO nanoparticles. *Superlattices Microstruct.* **2010**, *47*, 335-340, https://doi.org/10.1016/j.spmi.2009.11.007.
34. Ungula, J.; Dejene, B.F.; Swart, H.C. Effect of annealing on the structural, morphological and optical properties of Ga-doped ZnO nanoparticles by reflux precipitation method. *ResultsPphys.* **2017**, *7*, 2022-2027, https://doi.org/10.1016/j.rinp.2017.06.019.
35. Tuc Altaf, C.; Colak, T.O.; Rostas, A.M.; Popa, A.; Toloman, D.; Suciu, M.; Demirci Sankir, N.; Sankir, M. Impact on the Photocatalytic Dye Degradation of Morphology and Annealing-Induced Defects in Zinc Oxide Nanostructures. *ACS Omega* **2023**, *8*, 14952-14964, https://doi.org/10.1021/acsomega.2c07412.
36. Alrajhi, A.H.; Ahmed, N.M.; Halim, M.M.; Altowyan, A.S.; Azmi, M.N.; Almessiere, M.A. Distinct Optical and Structural (Nanoyarn and Nanomat-like Structure) Characteristics of Zinc Oxide Nanofilm Derived by Using *Salvia officinalis* Leaves Extract Made without and with PEO Polymer. *Materials* **2023**, *16*, 4510, https://doi.org/10.3390/ma16134510.
37. Lin, L.; Liu, J.; Lv, J.; Shen, S.; Wu, X.; Wu, D.; Qu, Y.; Zheng, W.; Lai, F. Correlation between native defects and morphological, structural and optical properties of ZnO nanostructures. *J. Alloys Compd.* **2017**, *695*, 1523-1527, https://doi.org/10.1016/j.jallcom.2016.10.292.
38. Schmidt-Mende, L.; MacManus-Driscoll, J.L. ZnO–nanostructures, defects, and devices. *Materialstoday* **2007**, *10*, 40-48, https://doi.org/10.1016/s1369-7021(07)70078-0.
39. Wu, J.-J.; Chen, G.-R.; Yang, H.-H.; Ku, C.-H.; Lai, J.-Y. Effects of dye adsorption on the electron transport properties in ZnO-nanowire dye-sensitized solar cells. *App. Phys. Lett.* **2007**, *90*, 213109, https://doi.org/10.1063/1.2742639.
40. Liu, K.; Sakurai, M.; Aono, M. ZnO-Based Ultraviolet Photodetectors. *Sensors* **2010**, *10*, 8604-8634, https://doi.org/10.3390/s100908604.
41. Osman, D.A.M.; Mustafa, M.A. Synthesis and Characterization of Zinc Oxide Nanoparticles using Zinc Acetate Dihydrate and Sodium Hydroxide. *J. Nanosci. Nanoeng.* **2015**, *1*, 248-251.
42. Santra, B.; Pal, S.; Saha, S.; Kanjilal, A. Tailoring Structural, Chemical, and Photocatalytic Properties of ZnO@β-SiC Composites: The Effect of Annealing Temperature and Environment. *ACS Omega* **2023**, *8*, 24113-24124, https://doi.org/10.1021/acsomega.3c03957.
43. Gegin, K.; Demir, A.; Öztürk, S.; Erkovan, M.; Kösemen, A. Boosting inverted type organic solar cell efficiency through the use of spray coated Y and Sn co-doped zinc oxide nanoparticles as an electron transport layers. *J. Mater. Sci. Mater. Electron.* **2023**, *34*, 1410, https://doi.org/10.1007/s10854-023-10739-6.
44. Radjehi, L.; Aissani, L.; Djelloul, A.; Saoudi, A.; Lamri, S.; Nomenyo, K.; Lerondel, G.; Sanchette, F. Air and Vacuum Annealing Effect on the Highly Conducting and Transparent Properties of the Undoped Zinc Oxide Thin Films Prepared by DC Magnetron Sputtering. *Metall. Mater. Eng.* **2023**, 29, 37-51, https://doi.org/10.56801/MME889.
45. Onwona-Agyeman, B.; Nakao, M.; Kumara, G.R.A. Photoelectrochemical solar cells made from $SnO_2$/ZnO films sensitized with an indoline dye. *J. Mater. Res.* **2010**, *25*, 1838-1841, https://doi.org/10.1557/jmr.2010.0235.
46. Tennakone, K.; Kumara, G.R.R.A.; Kottegoda, I.R.M.; Perera, V.P.S. An efficient dye-sensitized photoelectrochemical solar cell made from oxides of tin and zinc. *Chem. Commun.* **1999**, 15-16, https://doi.org/10.1039/a806801a.
47. Onwona-Agyeman, B.; Kaneko, S.; Kumara, A.; Okuya, M.; Murakami, K.; Konno, A.; Tennakone, K. Sensitization of Nanocrystalline $SnO_2$ Films with Indoline Dyes. *Jpn. J. Appl. Phys.* **2005**, *44*, L731, https://doi.org/10.1143/jjap.44.l731.
48. Velázquez-Nevárez, G.A.; Vargas-García, J.R.; Aguilar-Hernández, J.; Vega-Becerra, O.E.; Chen, F.; Shen, Q.; Zhang, L. Optical and Electrical Properties of (002)-Oriented ZnO Films Prepared on Amorphous Substrates by Sol-Gel Spin-Coating. *Mater. Res.* **2016**, *19*, 113-117, https://doi.org/10.1590/1980-5373-mr-2016-0808.
49. Bagabas, A.; Alshammari, A.; Aboud, M.F.; Kosslick, H. Room-temperature synthesis of zinc oxide nanoparticles in different media and their application in cyanide photodegradation. *Nanoscale Res.Lett.* **2013**, *8*, 516, https://doi.org/10.1186/1556-276x-8-516.

50. Raji, R.; Gopchandran, K.G. ZnO nanostructures with tunable visible luminescence: Effects of kinetics of chemical reduction and annealing. *J. Sci.: Adv. Mater. Dev.* **2017**, *2*, 51-58, https://doi.org/10.1016/j.jsamd.2017.02.002.
51. Zhu, S.; Shan, L.; Tian, X.; Zheng, X.; Sun, D.; Liu, X.; Wang, L.; Zhou, Z. Hydrothermal synthesis of oriented ZnO nanorod–nanosheets hierarchical architecture on zinc foil as flexible photoanodes for dye-sensitized solar cells. *Ceram. Int.* **2014**, *40*, 11663-11670, https://doi.org/10.1016/j.ceramint.2014.03.173.
52. Zhang, Q.; Liu, D.; Pei, H.; Pan, W.; Liu, Y.; Xu, S.; Cao, S. Swelling-reconstructed chitosan-viscose nonwoven fabric for high-performance quasi-solid-state supercapacitors. *J. Colloid Interface Sci.* **2022**, *617*, 489-499, https://doi.org/10.1016/j.jcis.2022.03.011.
53. Dutta, N.; Hazarika, S.; Maji, T.K. Study on the role of tannic acid–calcium oxide adduct as a green heat stabilizer as well as reinforcing filler in the bio-based hybrid polyvinyl chloride–thermoplastic starch polymer composite. *Polym. Eng. Sci.* **2021**, *61*, 2339-2348, https://doi.org/10.1002/pen.25761.
54. Bizzotto, F.; Quinson, J.; Schröder, J.; Zana, A.; Arenz, M. Surfactant-free colloidal strategies for highly dispersed and active supported $IrO_2$ catalysts: Synthesis and performance evaluation for the oxygen evolution reaction. *J.f Catal.* **2021**, *401*, 54-62, https://doi.org/10.1016/j.jcat.2021.07.004.
55. Fang, F.; Kennedy, J.; Futter, J.; Manning, J. A review of near infrared reflectance properties of metal oxide nanostructures. *GNS Science* **2013.**
56. Khorsand Zak, A.; Razali, R.; Abd Majid, W.H.; Darroudi, M. Synthesis and Characterization of a Narrow Size Distribution of Zinc Oxide Nanoparticles. *Int. J. Nanomedicine* **2011**, *6*, 1399–1403, https://doi.org/10.2147/ijn.s19693.
57. Morales, A.E.; Mora, E.S.; Pal, U. Use of Diffuse Reflectance Spectroscopy for Optical Characterization of Un-Supported Nanostructures. *Rev. Me. de Fís.* **2007**, *53*, 18-22.
58. Basu, K.; Benetti, D.; Zhao, H.; Jin, L.; Vetrone, F.; Vomiero, A.; Rosei, F. Enhanced photovoltaic properties in dye sensitized solar cells by surface treatment of $SnO_2$ photoanodes. *Sci. Rep.* **2016**, *6*, 23312, https://doi.org/10.1038/srep23312.
59. Gupta, P.; Ramrakhiani, M. Influence of the Particle Size on the Optical Properties of CdSe Nanoparticles. *Open Nanosci. J.* **2009**, *3*, 15-19, https://doi.org/10.2174/1874140100903010015.
60. Schwarzburg, K.; Willig, F. Influence of trap filling on photocurrent transients in polycrystalline $TiO_2$. *Appl. Phys. Lett.* **1991**, *58*, 2520-2522, https://doi.org/10.1063/1.104839.
61. Muñoz-García, A.B.; Benesperi, I.; Boschloo, G.; Concepcion, J.J.; Delcamp, J.H.; Gibson, E.A.; Meyer, G.J.; Pavone, M.; Pettersson, H.; Hagfeldt, A.; Freitag, M. Dye-sensitized solar cells strike back. *Chem. Soc. Rev.* **2021**, *50*, 12450-12550, https://doi.org/10.1039/d0cs01336f.
62. Emery, K.A. Solar simulators and *I–V* measurement methods. *Sol. Cells* **1986**, *18*, 251-260, https://doi.org/10.1016/0379-6787(86)90124-9.
63. Sutthana, S.; Hongsith, N.; Choopun, S. AZO/Ag/AZO multilayer films prepared by DC magnetron sputtering for dye-sensitized solar cell application. *Curr. Appl. Phys.* **2010**, *10*, 813-816, https://doi.org/10.1016/j.cap.2009.09.020.
64. Lee, S.-H.; Han, S.-H.; Jung, H.S.; Shin, H.; Lee, J.; Noh, J.-H.; Lee, S.; Cho, I.-S.; Lee, J.-K.; Kim, J.; Shin, H. Al-Doped ZnO Thin Film: A New Transparent Conducting Layer for ZnO Nanowire-Based Dye-Sensitized Solar Cells. *J. Phys. Chem. C* **2010**, *114*, 7185-7189, https://doi.org/10.1021/jp1008412.